

## Dirac line nodes and effect of spin-orbit coupling in the nonsymmorphic critical semimetals $MSiS$ ( $M = \text{Hf, Zr}$ )

C. Chen,<sup>1</sup> X. Xu,<sup>2</sup> J. Jiang,<sup>3,4,5</sup> S.-C. Wu,<sup>6</sup> Y. P. Qi,<sup>6</sup> L. X. Yang,<sup>2</sup> M. X. Wang,<sup>3</sup> Y. Sun,<sup>6</sup> N. B. M. Schröter,<sup>1</sup> H. F. Yang,<sup>1,3,7</sup> L. M. Schoop,<sup>8</sup> Y. Y. Lv,<sup>9</sup> J. Zhou,<sup>9</sup> Y. B. Chen,<sup>9</sup> S. H. Yao,<sup>9</sup> M. H. Lu,<sup>9</sup> Y. F. Chen,<sup>9</sup> C. Felser,<sup>6</sup> B. H. Yan,<sup>3,6</sup> Z. K. Liu,<sup>3,\*</sup> and Y. L. Chen<sup>1,2,3,†</sup>

<sup>1</sup>Department of Physics, University of Oxford, Oxford, OX1 3PU, United Kingdom

<sup>2</sup>State Key Laboratory of Low Dimensional Quantum Physics, Department of Physics, Tsinghua University, Beijing 100084, People's Republic of China

<sup>3</sup>School of Physical Science and Technology, ShanghaiTech University and Chinese Academy of Sciences-Shanghai Science Research Center, 393 Middle Huaxia Road, Shanghai 201210, People's Republic of China

<sup>4</sup>Advanced Light Source, Lawrence Berkeley National Laboratory, Berkeley, California 94720, USA

<sup>5</sup>Accelerator Laboratory, POSTECH, Pohang 790-784, Korea

<sup>6</sup>Max Planck Institute for Chemical Physics of Solids, D-01187 Dresden, Germany

<sup>7</sup>State Key Laboratory of Functional Materials for Informatics, SIMIT, Chinese Academy of Sciences, Shanghai 200050, People's Republic of China

<sup>8</sup>Max Planck Institute for Solid State Research, 70569 Stuttgart, Germany

<sup>9</sup>National Laboratory of Solid State Microstructures, School of Physics and Department of Materials Science and Engineering, Nanjing University, Nanjing, Jiangsu 210093, People's Republic of China

(Received 25 July 2016; revised manuscript received 14 December 2016; published 22 March 2017)

Topological Dirac semimetals (TDSs) represent a new state of quantum matter recently discovered that offers a platform for realizing many exotic physical phenomena. A TDS is characterized by the linear touching of bulk (conduction and valance) bands at discrete points in the momentum space [i.e., three-dimensional (3D) Dirac points], such as in  $\text{Na}_3\text{Bi}$  and  $\text{Cd}_3\text{As}_2$ . More recently, new types of Dirac semimetals with robust Dirac line nodes (with nontrivial topology or near the critical point between topological phase transitions) have been proposed that extend the bulk linear touching from discrete points to one-dimensional (1D) lines. In this paper, using angle-resolved photoemission spectroscopy (ARPES), we explored the electronic structure of the nonsymmorphic crystals  $MSiS$  ( $M = \text{Hf, Zr}$ ). Remarkably, by mapping out the band structure in the full 3D Brillouin zone (BZ), we observed two sets of Dirac line-nodes in parallel with the  $k_z$  axis and their dispersions. Interestingly, along directions other than the line nodes in the 3D BZ, the bulk degeneracy is lifted by spin-orbit coupling (SOC) in both compounds with larger magnitude in  $\text{HfSiS}$ . Our paper not only experimentally confirms a new Dirac line-node semimetal family protected by nonsymmorphic symmetry but also helps understanding and further exploring the exotic properties, as well as practical applications of the  $MSiS$  family of compounds.

DOI: [10.1103/PhysRevB.95.125126](https://doi.org/10.1103/PhysRevB.95.125126)

Topological Dirac semimetals (TDSs) are novel topological quantum materials that were recently discovered and intensively investigated for their rich physics and broad application potential [1–7]. Different from topological insulators (TIs), TDSs are characterized by the linear touching of bulk (instead of surface) bands. In the case of point touching, TDSs can naturally host three-dimensional (3D) Dirac fermions, making them the 3D analog of graphene with many exquisite transport properties, including high mobility charge carriers and large magnetoresistance [3,4]. Typically, in currently known TDSs (e.g.,  $\text{Na}_3\text{Bi}$  [1,3] and  $\text{Cd}_3\text{As}_2$  [2,4–7]), the 3D Dirac fermions are protected by time-reversal symmetry and inversion symmetry. With further symmetry breaking, these TDSs can evolve into more interesting topological states, e.g., to topological Weyl semimetals (TWSs) if time reversal or inversion symmetry is broken [8–10]. The TWSs represent another intensively investigated topological state with many interesting and unusual properties, such as unique surface Fermi arcs and the chiral magnetic effect [11–13].

More recently, a new type of TDS has been predicted in crystals with nonsymmorphic symmetry (such as glide planes or a screw axis) that induces a band degeneracy at the Brillouin zone (BZ) boundary, leading to one-dimensional (1D) Dirac line nodes [instead of discrete Dirac points (DPs) discussed above] [14]. The degeneracy at the line nodes is protected by nonsymmorphic symmetry and robust against perturbations, including spin-orbit coupling (SOC), which breaks the degeneracy along nodal rings in all previously discovered TDSs and TWSs (with the exception of the discrete Dirac or Weyl nodes) [10]. Moreover, compared to the discrete 3D DPs, 1D Dirac line nodes are a more significant feature in the band structure [Fig. 1(a)] and can have a stronger contribution to the physically observable properties of these materials (e.g., in electric transport) [15].

Although topological Dirac line-node semimetals (TDLS) have been predicted in various compounds, only a few of them have been experimentally studied, such as the  $MSiS$  ( $M = \text{Zr, Hf}$ ) family,  $\text{PbTaSe}_2$  and  $\text{PtSn}_4$ . Among them,  $\text{PbTaSe}_2$  is inversion asymmetric and hosts nodal rings protected by reflection symmetry under SOC. However, the various surface state (SS) bands interfering with the bulk features made the identification of nodal rings difficult [16].  $\text{PtSn}_4$  has

\*Corresponding author: liuzhk@shanghaitech.edu.cn

†Corresponding author: Yulin.Chen@physics.ox.ac.uk

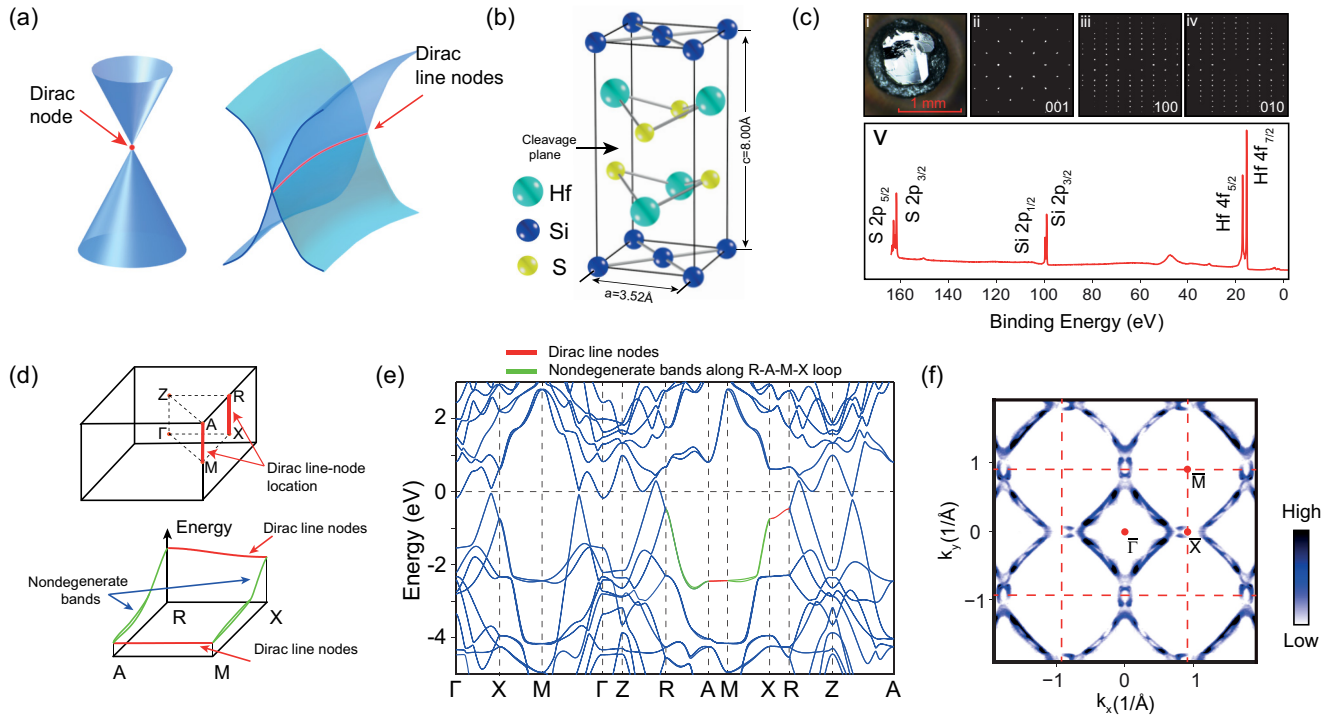


FIG. 1. Dirac line nodes and characterization of HfSiS single crystals. (a) Schematic illustration of Dirac node and Dirac line nodes in the momentum space. (b) Crystal structure of the HfSiS, showing the stacking of Si and Hf-S planes. Lattice constant and most probable cleavage plane is indicated. (c)(i) Photograph of the HfSiS crystal cleaved along (001) direction, (ii)–(iv) The XRD pattern of the (001), (100), and (010) surface of HfSiS and (v) core level spectrum of HfSiS showing characteristic  $S_{2p}$ ,  $Si_{2p}$ , and  $Hf_{4f}$  core level peaks. (d) Illustration of the Dirac line-node location (upper panel) and the dispersion of the line nodes (lower panel). (e) Calculation results of the bulk band structure of HfSiS along high-symmetry directions. Green lines indicate the positions where the bands are nondegenerate, while the red lines indicate the Dirac line nodes. (f) Broad range photoemission spectral intensity map of the FS covers nine BZs, showing the correct symmetry and the characteristic FS.

broken nodal arcs, and its topological character is still under investigation [17]; hence, it is also not a simple system to study. Due to its relatively simple electronic band structure, the  $MSiS$  family naturally becomes a suitable system for the investigation of TDLS. Although recent angle-resolved photoemission spectroscopy (ARPES) reports on ZrSiS [18–20] and the related compound ZrSnTe [21] have shown that bulk bands with linear dispersion exist (and the Dirac line nodes was suggested in Refs. [18, 19]), there has not yet been a systematic study in the full 3D BZ to demonstrate the Dirac line nodes and the dispersion in the momentum space. It, therefore, becomes the goal of this paper to clearly illustrate the Dirac line nodes and their detailed dispersions, discuss the TDLS nature, as well as to study the spin-orbit effect in different compounds of this family of materials.

In this investigation, by making use of high-resolution ARPES with broadly tunable photon energy, we systematically studied the electronic structure of two materials (HfSiS and ZrSiS) of the  $MSiS$  family compounds. By carrying out broad range momentum space and photon energy dependent measurements, we surveyed multiple BZs along all three momentum directions and were able to identify the electronic bands originating from both the bulk and SSs, which can be well reproduced by our (and previous) *ab initio* calculations [18–20]. Moreover, by tracking the Dirac band crossing along different high symmetry directions in the BZ, we clearly observed the Dirac line nodes along the  $X$ - $R$  and

$M$ - $A$  directions [see Figs. 1(d) and 1(e), red lines] and the lifting of the Dirac band degeneracy in other directions due to the SOC [Figs. 1(d) and 1(e), green lines]. The observation of the Dirac line nodes in HfSiS and ZrSiS thus proves the Dirac line-node semimetal nature of  $MSiS$  family of compounds, which have demonstrated many intriguing physical properties (e.g., high mobility electrons and “butterfly” shaped titanic angular magnetoresistance  $\sim 180\,000\%$  [15, 22–25]) and hints at its criticality to a topological nontrivial phase; thus, it can be an ideal platform for future investigations and applications.

Due to the larger SOC in HfSiS (compared to ZrSiS), we first focus on this compound. The crystal structure of HfSiS is illustrated in Fig. 1(b), clearly showing the Si-Hf/S-Hf/S trilayer layer structure (PbFCl structure type in the tetragonal  $P4/nmm$  space group (No. 129), with lattice constants  $a = b = 3.52 \text{ \AA}$ ,  $c = 8.00 \text{ \AA}$ ). Square nets of Si form glide planes in the crystal, while the  $C_{2x}(C_{2y})$  axis of the lattice are screw axes, thus preserving two kinds of nonsymmorphic symmetry. High quality single crystals were synthesized by iodine vapor transport (see Appendix: Materials and methods, part I for details). After cleaving, large (millimeter scale) flat and shiny surfaces are exposed [Fig. 1(c)(i)], which is ideal for ARPES measurements. The high quality of the crystal can be verified by the x-ray diffraction (XRD) measurements [Figs. 1(c)(ii)–1(c)(iv)]; and the core level photoemission spectrum clearly shows the characteristic  $Hf_{4f}$ ,  $S_{2p}$ , and  $Si_{2p}$  peaks [Fig. 1(c)(v)]. The *ab initio* calculated bulk band structure

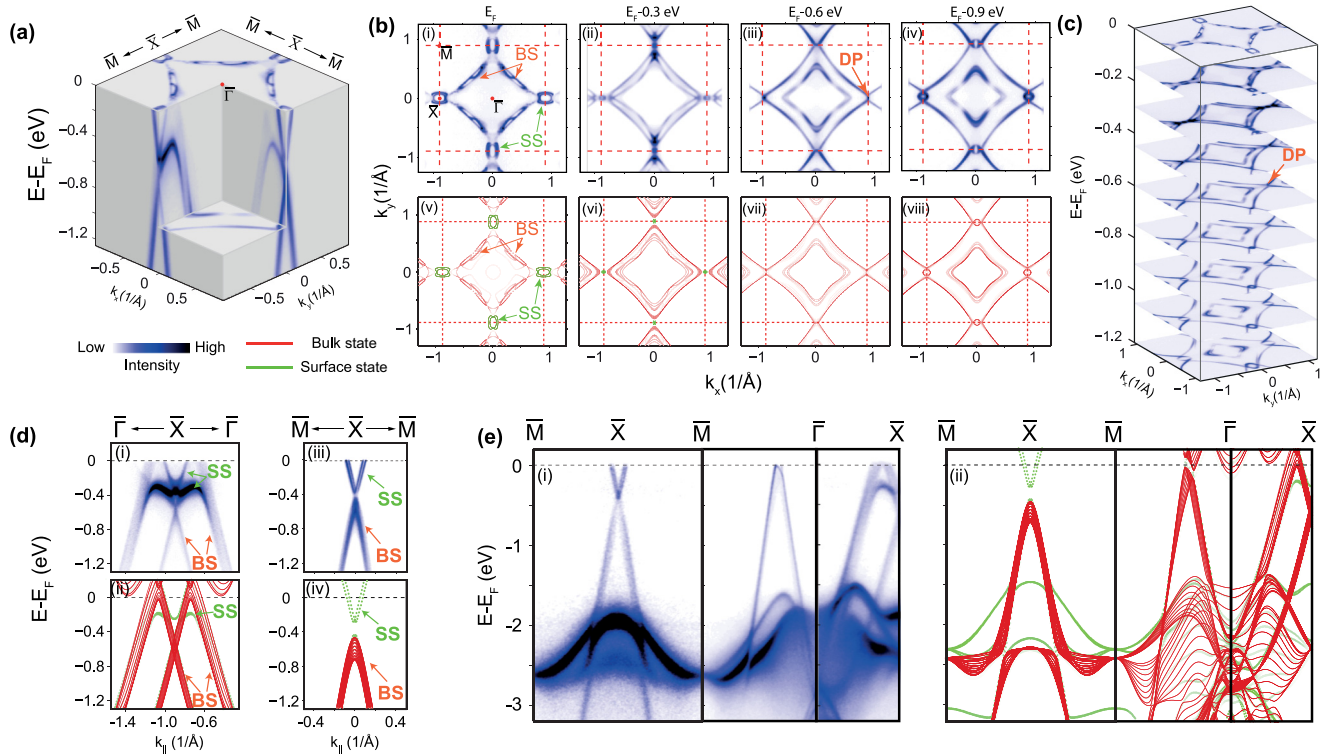


FIG. 2. General electronic structure of HfSiS. (a) The 3D intensity plot of the photoemission spectra centered around  $\bar{\Gamma}$ . (b) Top row: Photoemission spectral intensity map showing the constant energy contours of bands at  $E_B = 0$  (i), 0.3 eV (ii), 0.6 eV (iii), and 0.9 eV (iv), respectively. Bulk state, SS, and DP are labeled. Bottom row (v)–(viii): Corresponding calculated constant energy contours at the same binding energies as in experiments above. (c) Stacking plots of constant energy contours in broader binding energy range show the band structure evolution. The position of DP is labeled. (d) High symmetry cut along the  $\bar{\Gamma}$ - $\bar{X}$ - $\bar{\Gamma}$  (i) and  $\bar{M}$ - $\bar{X}$ - $\bar{M}$  (iii) directions near  $E_F$ , together with their corresponding calculated band structure (ii) and (iv). The BS and SS are labeled on the data and represented by red and green colors in the calculation. (e) Broad range high symmetry cut along the  $\bar{M}$ - $\bar{X}$ - $\bar{M}$ - $\bar{\Gamma}$ - $\bar{X}$  directions (i) and corresponding calculated band structure (ii). The BS and SS are represented by red and green colors in the calculation.

along high symmetry directions is shown in Fig. 1(e), where all the bands at  $X$  and  $M$  points are predicted to be at least doubly degenerate as the glide mirror symmetry  $\{M_z | \frac{1}{2}, \frac{1}{2}\}$  protects the band degeneracy at the  $X$  point and the screw axis symmetry  $\{C_{2x} | \frac{1}{2}, 0\}$  protects the band degeneracy at  $X$  and  $M$  point in the two-dimensional (2D) nonsymmorphic lattice within the  $P4/nmm$  group [14]. Extending to 3D, all lines along  $k_z$  ( $R$ - $X$ ,  $A$ - $M$ ) still preserve the same symmetries with the addition of inversion symmetry, thus forming degenerate lines, including the Dirac line nodes formed from the crossing of two Dirac-like bands [Figs. 1(d) and 1(e)]. The broad Fermi surface (FS) mapping in Fig. 1(f) covering multiple BZs confirmed the high quality (001) cleavage plane, which allows us to carry out the study below.

We, then, investigated the detailed electronic structure of HfSiS within a BZ with high-momentum and energy resolution, and an example is shown in Fig. 2. From the 3D plot of the overall band structure [Fig. 2(a)] and the constant energy contours [Figs. 2(b)(i)–2b(iv)], one could clearly identify two sets of features. One is the large diamond shaped FS, forming delicate structures connecting four  $\bar{X}$  points; and the other refers to the two concentric ellipses centred at each  $\bar{X}$  point. Both features [Figs. 2(b)(v)–2b(viii)] can be well reproduced by our *ab initio* calculations and previous reports [18–20],

which also helped us to identify their bulk (the diamond shape FS feature) and surface (the ellipses) origin, respectively (more discussion and the photon energy dependent ARPES measurements can be found below and in the Supplemental Material [26]).

For the concentric SS FSs around the  $\bar{X}$  points [see Figs. 2(b) and 2(c)], one can see that they are formed by a pair of Rashba split bands [the splitting is most apparent along  $\bar{M}$ - $\bar{X}$ - $\bar{M}$ ; see Fig. 2(d)(iii)], indicating the large SOC in HfSiS. The constant energy contours of this set of SS keep shrinking in size and eventually terminate at  $E_b \approx 0.4$  eV. Meanwhile, the linear bulk band dispersions [Figs. 2(b)(iii) and 2(d)(i)] form a DP ( $E_b \approx 0.6$  eV) at the  $\bar{X}$  point. We note that the slight broadening of the bulk band in Fig. 2(d)(i) is due to the  $k_z$  broadening effect [27], as can be clearly seen in the *ab initio* calculation [Fig. 2(d)(ii)], where the overlap of dispersions with different  $k_z$  momentum (red curves) cause slight broadening. The excellent overall agreement between the experiments [Figs. 2(d)(i), 2(d)(iii), and 2(e)(i)] and the calculation [Figs. 2(d)(ii), 2(d)(iv), and 2(e)(ii)] also allowed us to identify the additional SSs [green curves in Figs. 2d(ii), 2(d)(iv), and 2(e)(ii)] from the bulk states (BSs; more discussion about BS and SS at  $\bar{X}$  can be found in the Supplemental Material [26]), which simplified our

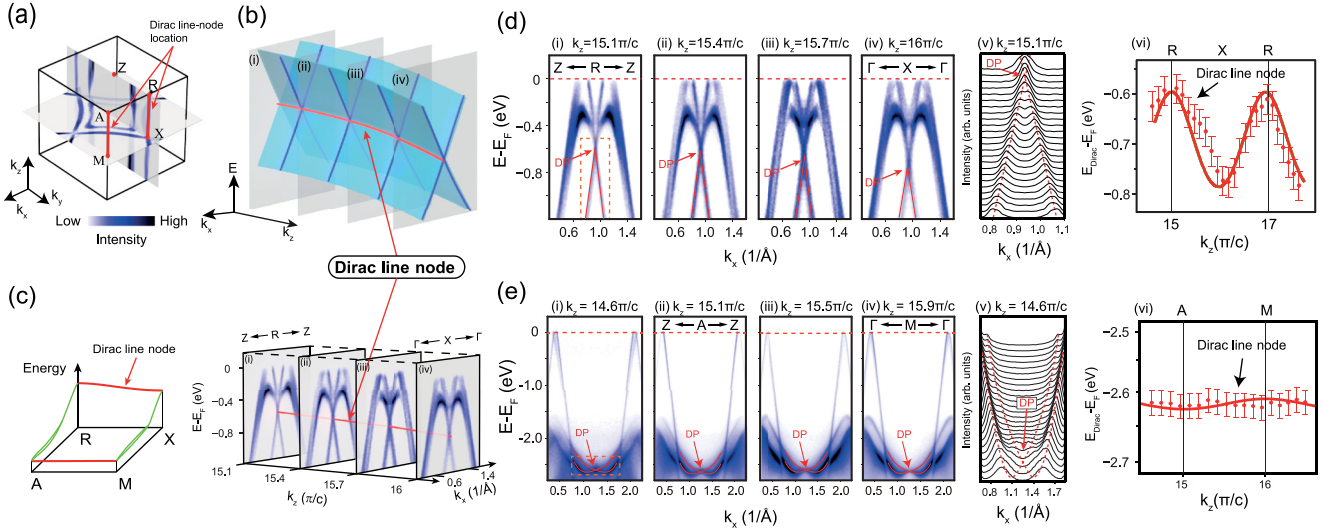


FIG. 3. Dirac line nodes in HfSiS. (a) Illustration of the location of Dirac line nodes in HfSiS. The 3D BZ also shows the constant energy contours in the  $k_y$ - $k_z$  plane (with  $k_x = 0$ ) and  $k_x$ - $k_y$  plane (with  $k_z = 0$ ) with energy around the DP. (b) Schematic of the band structure hosting a Dirac line node along the  $k_z$  direction. Grey planes represent locations where each cut in (c) is measured, and blue lines represent the Dirac dispersion we would observe in each cut. The Dirac line node is labeled by the red curve. (c) Left panel: schematic of the dispersion of the line node. Right panel: stack plot of the four cuts along  $(k_x, k_y) = (0, 0)$  to  $(k_x, k_y) = (0, \pi/a)$ , with  $k_z$  values ranging from 15 to  $16 \pi/c$ . Red curve indicate the Dirac line node. (d) (i)–(iv) Detailed analysis of the four cuts shown in (c) with the linear fitting results of the Dirac bands marked by red lines and DP labeled. (v) The Momentum Distribution Curve (MDC) plot for the region around the DP [indicated by the dashed box in (i)]. (vi) The fitting DP positions at various  $k_z$  values, with the red curve indicating the calculated dispersion along the  $R$ - $X$ - $R$  direction. (e) (i)–(iv) Plot and band fitting result of four cuts along  $(k_x, k_y) = (0, 0)$  to  $(k_x, k_y) = (\pi/a, \pi/a)$ , with  $k_z$  values ranging from 14.6 to  $16 \pi/c$ . Fitted parabolic dispersions and DP positions are labeled. (v) The MDC plot for the region around the DP [indicated by the dashed box in (i)]. (vi) The fitting DP positions at various  $k_z$  values, with the red curve indicating the calculated dispersion along the  $A$ - $M$ - $A$  direction.

investigation of the BSs and the identification of the bulk Dirac line node.

Next, we examine the dispersion of the Dirac node along different paths in the BZ. We first study the dispersion along  $X$ - $R$  direction [Fig. 3(a)] by conducting photon energy dependent ARPES (please see Supplemental Material [26] for more details on the determination of the  $k_z$  momentum). From a series of measurements at different  $k_z$  along  $(0, 0, k_z)(\pi/a, 0, k_z)$  direction [see Fig. 3(b) for a schematic illustration and Figs. 3(c) and 3(d) for sample measurements], we clearly observed that the Dirac node formed by linear band touching disperses with  $k_z$  and results in a line node along  $X$ - $R$  direction. With measurements of the fine  $k_z$  step, the dispersion of the  $X$ - $R$  line node could be reconstructed (by tracking the positions of the DP positions), as illustrated in Fig. 3(d)(v),

which shows good agreement with our calculations (solid red curve).

Similar to the  $X$ - $R$  line node, the predicted bulk band line node along the  $M$ - $A$  direction was also observed [caused by bulk Dirac crossings; see Figs. 1(e) and 3(e)(i)–3(e)(iv)], though with much less dispersion [Fig. 3(e)(v)]. The observation of the Dirac line node along  $X$ - $R$  and  $M$ - $A$  unambiguously confirms that HfSiS is a Dirac line-node semimetal.

Similarly, our measurement on ZrSiS have also obtained similar results on the Dirac line nodes (see Fig. 4), with the Dirac line node along  $X$ - $R$  and  $M$ - $A$  directions but with slightly weaker dispersion along the  $R$ - $X$ - $R$  direction [Fig. 4(c)].

Due to their similarity in their crystal structure, the comparison between the band structure of HfSiS and ZrSiS

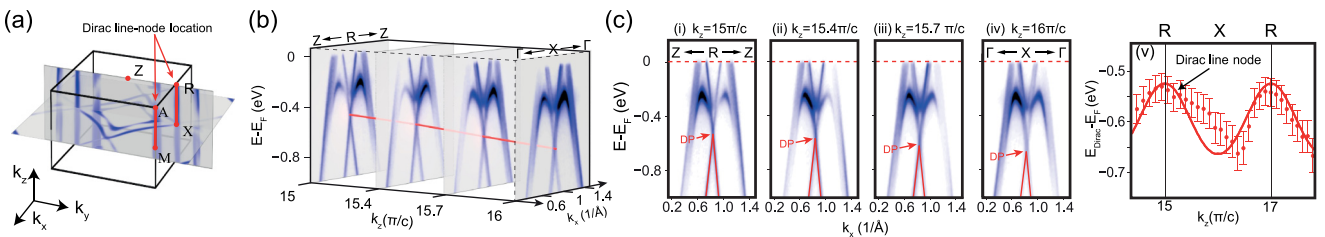


FIG. 4. Dirac line nodes in ZrSiS. (a) Illustration of the location of Dirac line nodes in ZrSiS. The 3D BZ also shows the constant energy contours in the  $k_y$ - $k_z$  plane (with  $k_x = 0$ ) and  $k_x$ - $k_y$  plane (with  $k_z = 0$ ) with energy around the DP. (b) Stack plot of the four cuts along  $(k_x, k_y) = (0, 0)$  to  $(k_x, k_y) = (0, \pi/a)$ , with  $k_z$  values ranging from 15 to  $16 \pi/c$ . Red curve indicates the Dirac line node. (c) (i)–(iv) Detailed analysis of the four cuts shown in (b) with the linear fitting results of the Dirac bands marked by red lines, and DP is labeled. (v) The fitting DP positions at various  $k_z$  values, with the red curve indicating the calculated dispersion along the  $R$ - $X$ - $R$  direction.

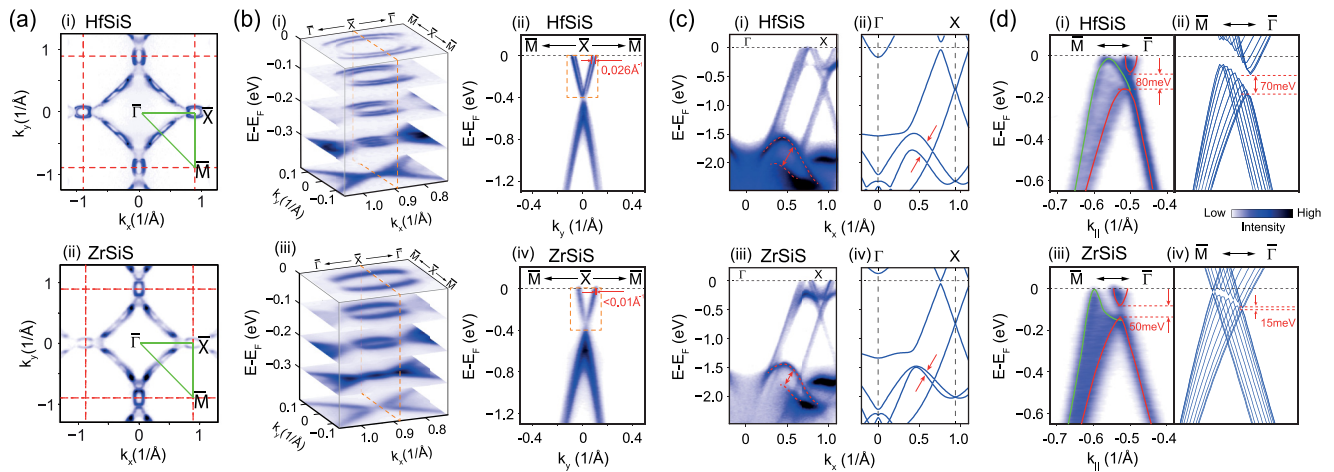


FIG. 5. Effect of SOC on the electronic structure of HfSiS and ZrSiS. (a) Constant energy contour on  $E_F$  of HfSiS (i) and ZrSiS (ii). Green lines indicate the cut directions in (b)–(d). (b) (i)–(ii) The 3D intensity plot of the photoemission spectra centered around  $\bar{X}$  and the high symmetry  $\bar{\Gamma}$ - $\bar{X}$  cut of HfSiS. (iii)–(iv) Same plot for ZrSiS. The SS splitting in both materials are estimated and labeled. (c) Comparison of the high symmetry  $\bar{\Gamma}$ - $\bar{X}$  cut together with the band structure calculation of HfSiS (i)–(ii) and ZrSiS (iii)–(iv). The band splitting in both materials are labeled. (d) Comparison of the high symmetry  $\bar{M}$ - $\bar{\Gamma}$  cut together with their band structure calculation of HfSiS (i) and (ii) and ZrSiS (iii) and (iv). In the spectrum, red curve labels the band structure at  $k_z = \pi$ , while the green curve labels the band structure from other  $k_z$  values. The band gap between the electron and hole pockets are estimated and labeled. In the calculation results, the band structure of all  $k_z$  values are plot together to reflect the uncertainty of  $k_z$  values each cut covers. The band splitting between the electron and hole pockets at  $k_z = \pi$  are labeled.

can provide important information about the effect of SOC in this family of Dirac line-node semimetals; one clear example is the effect on the SS around the  $\bar{X}$  point, where the two concentric pockets with a distinct separation can be seen in HfSiS [Figs. 5(b)(i) and 5b(ii)], the Rashba parameter estimated is 3.1 eVÅ; while the separation, if any, is smaller than our experimental resolution in ZrSiS [Figs. 5(b)(iii)–5b(iv)].

In addition to the SSs, the SOC also plays an important role in causing large bulk band splitting. As an example, along the  $\bar{\Gamma}$ - $\bar{X}$  direction [Fig. 5(c)], two bulk bands at high binding energy showing clearly larger splitting in HfSiS [Fig. 5(c)(i)] than that in ZrSiS [Fig. 5(c)(iii)], agreeing with our calculations [Figs. 5(c)(ii) and 5(c)(iv)] that also predict larger splitting in HfSiS. The effect of the SOC can also be seen at the crossing between the two Dirac-like bands halfway between  $\bar{\Gamma}$ - $\bar{M}$ , where the opening of a small band gap is also larger in HfSiS [ $\sim 80$  meV, see Fig. 4(d)(i)] than that in ZrSiS, [ $\sim 15$  meV, see Fig. 5(d)(iii)]. This is in contrast to the degenerate Dirac line nodes along  $\bar{X}$ - $\bar{R}$  and  $\bar{M}$ - $\bar{A}$  in the BZ, which are protected by the nonsymmorphic symmetry in both compounds.

Our systematic study on the electronic structures and the observation of their Dirac line nodes in  $MSiS$  ( $M = Zr, Hf$ ) family of compounds along the  $\bar{X}$ - $\bar{R}$  and  $\bar{M}$ - $\bar{A}$  directions (while the degeneracy is lifted in other directions) in the BZ clearly establish that these compounds are Dirac line-nodes semimetals protected by nonsymmorphic symmetry. The detailed characterization of the electronic structures of this family of compounds and the effect of the SOC will not only help us understand their intriguing transport properties, even if the DP observed is  $\sim 0.6$ – $0.8$  eV below  $E_F$  (e.g., the Dirac-like fermion contribution seen in the de Haas–van Alphen quantum oscillations [23], the nontrivial Berry phase and magnetoresistance [20,22,28], as well as the distinct

electron correlation effects due to the different energy scaling of the density of electronic states [29]) but also provide a solid base for designing and realizing exotic topological quantum phases and possible future applications with these materials. In particular, by tuning the DP of the  $MSiS$  materials to the  $E_F$  vicinity, these materials may lead to more interesting discovery in the transport properties from the Dirac line-nodes semimetals.

Finally, although the theoretical calculations so far suggest that these two compounds do not have nontrivial topology, there are gathering transport and photoemission evidences that strongly suggest a topologically nontrivial phase in the  $MSiS$  family [19–25,28,30]. In addition, the family compounds are close to the border of the topological phase transition; and many materials with the same crystal structures have rich topologically nontrivial phases, such as (nonsymmorphic symmetry protected) TIs and topological semimetals [31,32]. The application of external influence, such as mechanical strain or chemical substitution, further opens up the opportunity to drive the topological phase transition of  $MSiS$  materials. Thus, we conclude the  $MSiS$  material is at least a topologically critical line-node semimetal and believe the study of these materials will be important for the systematic study of the topological phase diagram and the associated topological phase transitions of the  $MSiS$  and relevant compounds.

As we were preparing this paper, we noticed an ARPES report has also addressed the surface band splitting due to the stronger SOC strength in HfSiS [30].

This work is supported by grant from Chinese Academy of Science-Shanghai Science Research Center, Grant No: CAS-SSRC-YH-2015-01. Y.L.C. acknowledges the support from the Engineering and Physical Sciences Research Council Platform Grant (Grant No. EP/M020517/1) and Hefei Science

Center Chinese Academy of Sciences (2015HSC-UE013). Z.K.L. acknowledges the support from the National Natural Science Foundation of China (11674229). C.F. acknowledges financial support from the European Research Council Advanced Grant (No. 291472 Idea Heusler). C.C. acknowledges the support of the China Scholarship Council–University of Oxford Scholarship. J.J. acknowledges the support of the National Research Foundation, Korea, through the SRC Center for Topological Matter (No. 2011-0030787). H.F.Y. acknowledges financial support from the Bureau of Frontier Sciences and Education, Chinese Academy of Sciences. N.B.M.S. acknowledges the support from Studienstiftung des deutschen Volkes. Y.L.C. conceived the experiments. C.C. and Z.K.L. carried out angle-resolved photoemission spectroscopy measurements, with the assistance of J.J., L.X.Y., and M.X.W. Y.P.Q. and S.H.Y. synthesized and characterized the bulk single crystals. S.C.W., Y.S., J.Z., and B.H.Y. performed *ab initio* calculations. All authors contributed to the scientific planning and discussions. The authors declare no competing financial interests.

C.C. and X.X. contributed equally to this work.

## APPENDIX: MATERIALS AND METHODS

### 1. Sample synthesis

Single crystals of HfSiS were grown via iodine ( $I_2$ ) vapor transport in a two step process. At first, the polycrystalline HfSiS powder was synthesized using a high-purity elemental Hf piece, Si piece, S powder in a process described elsewhere [33]. Then, the polycrystalline powder together with iodine were sealed in a quartz tube under vacuum. The quartz

tube was then kept in a gradient furnace for 10 days with the powder at  $1100^\circ\text{C}$ , while the cooler end was kept at  $1000^\circ\text{C}$ . Shiny rectangular platelike crystals were obtained at the cooler end for ARPES measurements.

### 2. Angle-resolved photoemission spectroscopy

The ARPES measurements were performed at the beamline I05 of the Diamond Light Source (DLS) and beamline 13U of the National Synchrotron Radiation Laboratory (NSRL), Hefei, People's Republic of China, both equipped with Scienta R4000 analyzers. The measurement sample temperature and pressure were 10 K and lower than  $1.5 \times 10^{-10}$  Torr, respectively. The angle resolution was  $0.2^\circ$ , and the overall energy resolutions were better than 15 meV. The samples were cleaved *in situ* along the (001) plane.

### 3. *Ab initio* calculations

The density functional theory (DFT) calculations were performed by using the Vienna *Ab initio* Simulation Package (VASP) with the projected-augmented wave method (PAW) [34]. The exchange and correlation energy was considered in the generalized gradient approximation (GGA) with Perdew-Burke-Ernzerhof (PBE) based density functional [35]. The energy cutoff was set to 259 eV. Experimental lattice constants were used for two compounds in all the calculations. A (001) slab model of five bulk units thick ( $40 \text{ \AA}$ ) was constructed with the periodicity in the  $xy$  plane and a vacuum layer of  $20 \text{ \AA}$  in the  $z$  direction to simulate the (001) surface. The slab band structure was projected to the atomic orbitals of the one unit cell on the top to identify the SSs.

- 
- [1] Z. Wang, Y. Sun, X.-Q. Chen, C. Franchini, G. Xu, H. Weng, X. Dai, and Z. Fang, Dirac semimetal and topological phase transitions in  $A_3\text{Bi}$  ( $A = \text{Na, K, Rb}$ ), *Phys. Rev. B* **85**, 195320 (2012).
- [2] Z. Wang, H. Weng, Q. Wu, X. Dai, and Z. Fang, Three-dimensional Dirac semimetal and quantum transport in  $\text{Cd}_3\text{As}_2$ , *Phys. Rev. B* **88**, 125427 (2013).
- [3] Z. K. Liu, B. Zhou, Y. Zhang, Z. J. Wang, H. M. Weng, D. Prabhakaran, S. K. Mo, Z. X. Shen, Z. Fang, X. Dai, Z. Hussain, and Y. L. Chen, Discovery of a three-dimensional topological Dirac semimetal,  $\text{Na}_3\text{Bi}$ , *Science* **343**, 864 (2014).
- [4] Z. K. Liu, J. Jiang, B. Zhou, Z. J. Wang, Y. Zhang, H. M. Weng, D. Prabhakaran, S. K. Mo, H. Peng, P. Dudin, T. Kim, M. Hoesch, Z. Fang, X. Dai, Z. X. Shen, D. L. Feng, Z. Hussain, and Y. L. Chen, A stable three-dimensional topological Dirac semimetal  $\text{Cd}_3\text{As}_2$ , *Nat. Mater.* **13**, 677 (2014).
- [5] M. Neupane, S.-Y. Xu, R. Sankar, N. Alidoust, G. Bian, C. Liu, I. Belopolski, T.-R. Chang, H.-T. Jeng, H. Lin, A. Bansil, F. Chou, and M. Z. Hasan, Observation of a three-dimensional topological Dirac semimetal phase in high-mobility  $\text{Cd}_3\text{As}_2$ , *Nat. Commun.* **5**, 3786 (2014).
- [6] M. N. Ali, Q. Gibson, S. Jeon, B. B. Zhou, A. Yazdani, and R. J. Cava, The crystal and electronic structures of  $\text{Cd}_3\text{As}_2$ , the three-dimensional electronic analogue of graphene, *Inorg. Chem.* **53**, 4062 (2014).
- [7] S. Borisenko, Q. Gibson, D. Evtushinsky, V. Zabolotnyy, B. Büchner, and R. J. Cava, Experimental Realization of a Three-Dimensional Dirac Semimetal, *Phys. Rev. Lett.* **113**, 027603 (2014).
- [8] X. Wan, A. M. Turner, A. Vishwanath, and S. Y. Savrasov, Topological semimetal and Fermi-arc surface states in the electronic structure of pyrochlore iridates, *Phys. Rev. B* **83**, 205101 (2011).
- [9] S. Jeon, B. B. Zhou, A. Gyenis, B. E. Feldman, I. Kimchi, A. C. Potter, Q. D. Gibson, R. J. Cava, A. Vishwanath, and A. Yazdani, Landau quantization and quasiparticle interference in the three-dimensional Dirac semimetal  $\text{Cd}_3\text{As}_2$ , *Nat. Mater.* **13**, 851 (2014).
- [10] H. Weng, C. Fang, Z. Fang, B. A. Bernevig, and X. Dai, Weyl Semimetal Phase in Noncentrosymmetric Transition-Metal Monophosphides, *Phys. Rev. X* **5**, 011029 (2015).
- [11] B. Q. Lv, N. Xu, H. M. Weng, J. Z. Ma, P. Richard, X. C. Huang, L. X. Zhao, G. F. Chen, C. E. Matt, F. Bisti, V. N. Strocov, J. Mesot, Z. Fang, X. Dai, T. Qian, M. Shi, and H. Ding, Observation of Weyl nodes in TaAs, *Nat. Phys.* **11**, 724 (2015).

- [12] S.-Y. Xu, I. Belopolski, N. Alidoust, M. Neupane, G. Bian, C. Zhang, R. Sankar, G. Chang, Z. Yuan, C.-C. Lee, S.-M. Huang, H. Zheng, J. Ma, D. S. Sanchez, B. Wang, A. Bansil, F. Chou, P. P. Shibayev, H. Lin, S. Jia, and M. Z. Hasan, Discovery of a Weyl fermion semimetal and topological Fermi arcs, *Science* **349**, 613 (2015).
- [13] L. X. Yang, Z. K. Liu, Y. Sun, H. Peng, H. F. Yang, T. Zhang, B. Zhou, Y. Zhang, Y. F. Guo, M. Rahn, D. Prabhakaran, Z. Hussain, S. K. Mo, C. Felser, B. Yan, and Y. L. Chen, Weyl semimetal phase in the non-centrosymmetric compound TaAs, *Nat. Phys.* **11**, 728 (2015).
- [14] S. M. Young and C. L. Kane, Dirac Semimetal in Two Dimensions, *Phys. Rev. Lett.* **115**, 126803 (2015).
- [15] M. N. Ali, L. M. Schoop, C. Garg, J. M. Lippmann, E. Lara, B. Lotsch, and S. S. P. Parkin, Butterfly magnetoresistance, quasi-2D Dirac Fermi surface and topological phase transition in ZrSiS, *Science Advances* **2**, e1601742 (2016).
- [16] G. Bian, T.-R. Chang, R. Sankar, S.-Y. Xu, H. Zheng, T. Neupert, C.-K. Chiu, S.-M. Huang, G. Chang, I. Belopolski, D. S. Sanchez, M. Neupane, N. Alidoust, C. Liu, B. Wang, C.-C. Lee, H.-T. Jeng, C. Zhang, Z. Yuan, S. Jia, A. Bansil *et al.*, Topological nodal-line fermions in spin-orbit metal PbTaSe<sub>2</sub>, *Nat. Commun.* **7**, 10556 (2016).
- [17] Y. Wu, L.-L. Wang, E. Mun, D. D. Johnson, D. Mou, L. Huang, Y. Lee, S. L. Bud'ko, P. C. Canfield, and A. Kaminski, Dirac node arcs in PtSn<sub>4</sub>, *Nat. Phys.* **12**, 667 (2016).
- [18] L. M. Schoop, M. N. Ali, C. Straßer, A. Topp, A. Varykhalov, D. Marchenko, V. Duppel, S. S. P. Parkin, B. V. Lotsch, and C. R. Ast, Dirac cone protected by non-symmorphic symmetry and three-dimensional Dirac line node in ZrSiS, *Nat. Commun.* **7**, 11696 (2016).
- [19] M. Neupane, I. Belopolski, M. M. Hosen, D. S. Sanchez, R. Sankar, M. Szlowska, S.-Y. Xu, K. Dimitri, N. Dhakal, P. Maldonado, P. M. Oppeneer, D. Kaczorowski, F. Chou, M. Z. Hasan, and T. Durakiewicz, Observation of topological nodal fermion semimetal phase in ZrSiS, *Phys. Rev. B* **93**, 201104 (2016).
- [20] X. Wang, X. Pan, M. Gao, J. Yu, J. Jiang, J. Zhang, H. Zuo, M. Zhang, Z. Wei, W. Niu, Z. Xia, X. Wan, Y. Chen, F. Song, Y. Xu, B. Wang, G. Wang, and R. Zhang, Evidence of both surface and bulk Dirac bands and anisotropic nonsaturating magnetoresistance in ZrSiS, *Adv. Electron. Mater.* **2**, 1600228 (2016).
- [21] R. Lou, J.-Z. Ma, Q.-N. Xu, B.-B. Fu, L.-Y. Kong, Y.-G. Shi, P. Richard, H.-M. Weng, Z. Fang, S.-S. Sun, Q. Wang, H.-C. Lei, T. Qian, H. Ding, and S.-C. Wang, Emergence of topological bands on the surface of ZrSnTe crystal, *Phys. Rev. B* **93**, 241104 (2016).
- [22] R. Singha, A. K. Pariari, B. Satpati, and P. Mandal, Large non-saturating magnetoresistance and signature of nondegenerate Dirac nodes in ZrSiS, *Proc. Natl. Acad. Sci. USA* **114**, 2468 (2017).
- [23] J. Hu, Z. Tang, J. Liu, X. Liu, Y. Zhu, D. Graf, K. Myhro, S. Tran, C. N. Lau, J. Wei, and Z. Mao, Evidence of Topological Nodal-Line Fermions in ZrSiSe and ZrSiTe, *Phys. Rev. Lett.* **117**, 016602 (2016).
- [24] Y.-Y. Lv, B.-B. Zhang, X. Li, S.-H. Yao, Y. B. Chen, J. Zhou, S.-T. Zhang, M.-H. Lu and Y.-F. Chen, Extremely large and significantly anisotropic magnetoresistance in ZrSiS single crystals, *Appl. Phys. Lett.* **108**, 244101 (2016).
- [25] J. Hu, Z. Tang, J. Liu, Y. Zhu, J. Wei, and Z. Mao, Evidence of Dirac cones with 3D character probed by dHvA oscillations in nodal-line semimetal ZrSiS, [arXiv:1604.01567](https://arxiv.org/abs/1604.01567).
- [26] See Supplemental Material at <http://link.aps.org/supplemental/10.1103/PhysRevB.95.125126> for details on the  $k_z$  dispersion of the bandstructure, as well as the fitting procedures for the Dirac point.
- [27] V. N. Strocov, Intrinsic accuracy in 3-dimensional photoemission band mapping, *J. Electron Spectrosc. Relat. Phenom.* **130**, 65 (2003).
- [28] N. Kumar, K. Manna, Y. P. Qi, S.-C. Wu, L. Wang, B. H. Yan, C. Felser, and C. Shekhar, Unusual magnetotransport from Si-square nets in topological semimetal HfSiS, [arXiv:1612.05176](https://arxiv.org/abs/1612.05176).
- [29] Y. Huh, E. G. Moon, and Y.-B. Kim, Long-range Coulomb interaction in nodal-ring semimetals, *Phys. Rev. B* **93**, 035138 (2016).
- [30] D. Takane, Z. W. Wang, S. Souma, K. Nakayama, C. X. Trang, T. Sato, T. Takahashi, and Y. Ando, Dirac-node arc in the topological line-node semimetal HfSiS, *Phys. Rev. B* **94**, 121108 (2016).
- [31] Q. Xu, Z. Song, S. Nie, H. M. Weng, Z. Fang, and X. Dai, Two-dimensional oxide topological insulator with iron-pnictide superconductor LiFeAs structure, *Phys. Rev. B* **92**, 205310 (2015).
- [32] C. Le, S. Qin, X. Wu, X. Dai, P. Fu, and J. Hu, Three-dimensional critical Dirac semimetal in KMgBi, [arXiv:1606.05042](https://arxiv.org/abs/1606.05042).
- [33] A. K. Haneveld and F. Jellinek, Zirconium silicide and germanide chalcogenides preparation and crystal structures, *Recl. Trav. Chim.* **83**, 776 (1964).
- [34] G. Kresse and J. Hafner, *Ab initio* molecular dynamics for open-shell transition metals, *Phys. Rev. B* **48**, 13115 (1993).
- [35] J. P. Perdew, K. Burke, and M. Ernzerhof, Generalized Gradient Approximation Made Simple, *Phys. Rev. Lett.* **77**, 3865 (1996).